Retrieving Soil and Vegetation Temperatures From Dual-Angle and Multipixel Satellite Observations

Zunjian Bian, Hua Li, Frank M. Göttsche, Ruibo Li, Yongming Du, Huazhong Ren, Biao Cao, Qing Xiao, and Qinhuo Liu

***Abstract*—Land surface component temperatures (LSCTs), i.e., the temperatures of soil and vegetation, are important parameters in many applications, such as estimating evapotranspiration and monitoring droughts. However, the multiangle algorithm is affected due to different spatial resolution between nadir and oblique views. Therefore, we propose a combined retrieval algorithm that uses dual-angle and multipixel observations together. The sea and land surface temperature radiometer onboard ESA's Sentinel-3 satellite allows for quasi-synchronous dual-angle observations, from which LSCTs can be retrieved using dual-angle and multipixel algorithms. The better performance of the combined algorithm is demonstrated using a sensitivity analysis based on a synthetic dataset. The spatial errors in the oblique view due to different spatial resolution can reach 4.5 K and have a large effect on the multiangle algorithm. The introduction of multipixel information in a window can reduce the effect of such spatial errors, and the retrieval results of LSCTs can be further improved by using multiangle information for a pixel. In the validation, the proposed combined algorithm performed better, with LSCT root mean squared errors of 3.09 K and 1.91 K for soil and vegetation at a grass site, respectively, and corresponding values of 3.71 K and 3.42 K at a sparse forest site, respectively. Considering that the temperature differences between components can reach 20 K, the results confirm that, in addition to a pixel-average LST, the combined retrieval algorithm can provide information on LSCTs. This article demonstrates the potential of utilizing additional information sources for better LSCT results, which makes the presented combined strategy a promising option for deriving large-scale LSCT products.**

***Index Terms*—Bayesian strategy, land surface temperature (LST), multiangle and multipixel LST retrieval, sea and land surface temperature radiometer (SLSTR) data, soil and vegetation component temperatures.**

I. Introduction

LAND surface temperature (LST) is a key parameter in surface physical processes, such as the energy budget and water cycle, and plays an essential role in applications, such as weather prediction, surface drought monitoring and agricultural yield estimation [1]–[3]. In the last three decades, a dramatic development has occurred in LST retrieval from satellite data, including the following algorithms: single-channel [4], two-channel split-window (SW) [5], Day/Night algorithm [6], and temperature emissivity separation [7], [8]. Moreover, various LST products have been generated at both local and global scales [1]. One of the main limitations of these products is that the retrieved LST reflects only pixel-average temperatures rather than physical temperatures of land surface components, such as soil and vegetation. Mixed pixels with apparently isothermal components usually occur because the spatial resolution of geostationary and polar-orbit satellites is approximately 1.0–5.0 km. For spatially coarse satellite data, knowledge of the land surface component temperatures (LSCTs) in a pixel seems more desirable for accurately recording the surface temperature state. Moreover, there are numerous studies describing the usefulness of LSCT in applications, e.g., for improved estimates of evapotranspiration with a two-source energy balance model [9] drought monitoring with a modified temperature vegetation dryness index [10], and vegetation growth monitoring with a crop water stress index [11].

A number of radiative transfer models have been proposed to explain the physical relationship between LSCTs and thermal infrared (TIR) observations [12]–[15], which can be considered a prerequisite for LSCT retrieval. Based on these approaches, a large part of previous LSCT research focused on obtaining more accurate results by introducing more complex models [16], [17]. However, recent studies have concluded that practical and robust algorithms may be more useful for retrieving LSCTs from satellite data. A considerable amount of literature has focused on such algorithms and has been published for different types of TIR observations. The respective literature was reviewed by Zhan *et al*. [18], who classified LSCT retrieval algorithms into four types: multiangle, multichannel, multitemporal, and multipixel/multiresolution algorithms. However, to the best of our

Manuscript received May 22, 2020; revised August 12, 2020; accepted September 9, 2020. Date of publication September 15, 2020; date of current version September 28, 2020. This work was supported in part by the Chinese Natural Science Foundation Project under Grant 41671366 and Grant 41930111, in part by the National Key Research and Development Program of China under Grant 2018YFA0605503, in part by Project funded by China Postdoctoral Science Foundation (BX20190364, 2019M650037), in part by Chinese Natural Science Foundation Project (41901287, 41871258), in part by the Youth Innovation Promotion Association CAS under Grant 2020127, and in part by the "Future Star" Talent Plan of the Aerospace Information Research Institute of Chinese Academy of Sciences under Grant Y920570Z1F. *(Corresponding author: Hua Li.)*

Zunjian Bian, Hua Li, Yongming Du, Biao Cao, Qing Xiao, and Qinhuo Liu are with the State Key Laboratory of Remote Sensing Science, Aerospace Information Research Institute of Chinese Academy of Sciences, Beijing 100101, China (e-mail: bianzj@aircas.ac.cn; lihua@radi.ac.cn; duym@radi.ac.cn; caobiao@aircas.ac.cn; xiaoqing@radi.ac.cn; liuqh@radi.ac.cn).

Frank M. Göttsche is with the Karlsruhe Institute of Technology, IMK-ASF, Hermann-von-Helmholtz-Platz 1, 76344 Eggenstein-Leopoldshafen, Germany (e-mail: frank.goettsche@kit.edu).

Ruibo Li is with the College of Geomatics, Shandong University of Science and Technology, Qingdao 266590, China (e-mail: lrb0106@sdust.edu.cn).

Huazhong Ren is with the Institute of RS and GIS, Peking University, Beijing 100871, China (e-mail: renhuazhong@pku.edu.cn).

Digital Object Identifier 10.1109/JSTARS.2020.3024190

knowledge, no practical algorithm for retrieving LSCTs from satellite data yet exists that is sufficiently robust to be integrated into an operational processing chain. So far, all multichannel algorithms have suffered from high autocorrelation between the observations, which is due to slight differences in TIR emissivity between soil and vegetation [19]. Similar complications are faced by multipixel/multiresolution algorithms over relatively homogeneous surfaces [20]. An ill-posed problem may occur for the multitemporal algorithm because two or more unknown LSCTs are introduced when one observation at different times is added [21]. Relative to the abovementioned algorithms, the multiangle algorithm has received the most attention and has generally been identified as a good tool [12]. The feasibility and limitations of LSCT retrieval from along track scanning radiometer (ATSR) data were described in [22]. Li *et al*. [23] and Jia *et al.* [24] succeeded in retrieving soil and vegetation temperatures using dual-angle LSTs that were retrieved with an SW algorithm applied to ATSR series data. The difficulties in LSCT retrieval not only are due to uncertainty in atmospheric correction and fractional vegetation cover (FVC) but also are caused by differences in spatial resolution between nadir and oblique views, particularly over heterogeneous surfaces [25].

Considering the characteristics of the various algorithms, a joint application of several algorithms may be helpful for a multiangle algorithm, particularly for the effect of different spatial resolution between nadir and oblique views. Furthermore, there has been considerable progress in the availability of suitable satellite data: the sea and land surface temperature radiometers (SLSTRs) onboard Sentinel-3 A and B satellites (launched in February 2016 and April 2018, respectively) provide quasi-synchronous dual-angle observations and continuity for the Advanced ATSR. Thanks to this new data source, LSCT retrievals with multiangle and multipixel algorithms have become considerably more feasible. Therefore, it is desirable to make full use of SLSTR observations and to explore suitable strategies for combining the two algorithms so that robust LSCT estimates can be obtained.

In this article, we explore an LSCT retrieval to use SLSTR multiangle and multipixel observations together. The combined retrieval algorithm is evaluated with surface measurements from two sites covered by grass and sparse forest canopies, respectively. Furthermore, the combined algorithm has been analyzed using a synthetic dataset for the Heihe River Basin and comparisons with the individual multiangle algorithm. The outline of this article is as follows. Section II considers the study area and data sources, which include satellite data and surface measurements. Section III describes LSCT retrieval with multiangle and multipixel algorithms. Section IV provides analysis results obtained for a synthetic dataset and validates retrieved LSCT results with surface measurements. Section V discusses the limitations of the evaluation and retrieval procedure. Finally, Section VI presents a short summary and provides the conclusion.

II. Materials

A. Input SLSTR Data

In this study, LSCT retrieval was performed using SLSTR dual-angle data. SLSTR is a dual scan temperature radiometer, which has been selected for the low earth orbit (800–830 km altitude) ESA Sentinel-3 operational mission as a part of the Copernicus Program [26]. The planned period of operation is 20 years. The wavelength range of SLSTR encompasses the visible and near-infrared (VNIR, 0.555, 0.659, and 0.865 μm), shortwave infrared (SWIR, 1.375, 1.61, and 2.25 μm), TIR (3.74, 10.85, and 12.0 μm), and TIR fire (TIRf, 3.74 and 10.85 μm) bands. The spatial resolution of the VNIR/SWIR and TIR data were regridded to 500 and 1000 m in the SLSTR level-1 product, respectively. To date, a number of studies have reported practical applications of the SLSTR data [27]. The data used in this study were obtained from Sentinel 3A. While Sentinel 3A data are obtained each day, dual-angle data are obtained only approximately every 4 days, since, in oblique view, the swath across the track ($\sim$740 km) is smaller than in nadir view ($\sim$1400 km).

Currently, SLSTR level-2 LST products associated with the nadir view are officially provided. The retrieval of this product also utilizes Sentinel-3 Ocean and Land Color Imager (OLCI) data and Sentinel-2 Multi-Spectral Instrument (MSI) data [28]. Here, SLSTR level-2 LST is not used because the analysis of the retrieved LSCT is more consistent and intuitive if nadir and oblique LSTs are obtained by a single algorithm. The vegetation growing season, which in the studied regions lasts approximately from day of year (DOY) 120 to 270 of 2017, was selected. Only daytime data were used because at nighttime, temperature differences between land surface components are usually small. Cloud and water vapor content (WVC) information was extracted from SLSTR level-1 products [29].

B. Input Emissivity Data

For each pixel, the emissivity of its soil and vegetation components and its canopy must be known before the corresponding LSCTs can be retrieved. In this study, soil and vegetation emissivity were input, and canopy (=pixel effective) emissivity was calculated using the vegetation cover fraction method [28], which is based on the normalized difference vegetation index (NDVI) [30]

$$\varepsilon_i = f_s\, \varepsilon_{s,i} + f_v \varepsilon_{v,i} + d\varepsilon \tag{1}$$

$$f_v = \frac{\mathrm{NDVI} - \mathrm{NDVI}_s}{\mathrm{NDVI}_v - \mathrm{NDVI}_s} \tag{2}$$

$$f_s = 1 - f_v \tag{3}$$

where $\varepsilon_{s,i}$, $\varepsilon_{v,i}$, and ε_i represent the soil, vegetation, and canopy emissivity for SLSTR channel $i = 8,\ 9$, respectively; f_s and f_v represent the visible proportion of soil and vegetation, respectively; and $d\varepsilon$ represents a cavity term, which accounts for multiple scattering effects. NDVI_s and NDVI_v represent the NDVI values for bare soil and fully vegetated surfaces: based on statistics in this study, they were set to 0.061 and 0.947, respectively. The soil emissivity ε_s was set pixel by pixel based on a reference background emissivity, which was obtained from the physically retrieved ASTER GEDv3 emissivity product [31]. The vegetation emissivity ε_v was set for each surface class in the MODIS IGBP land cover type product. Detailed information about the LSE calculation can be found in [30].

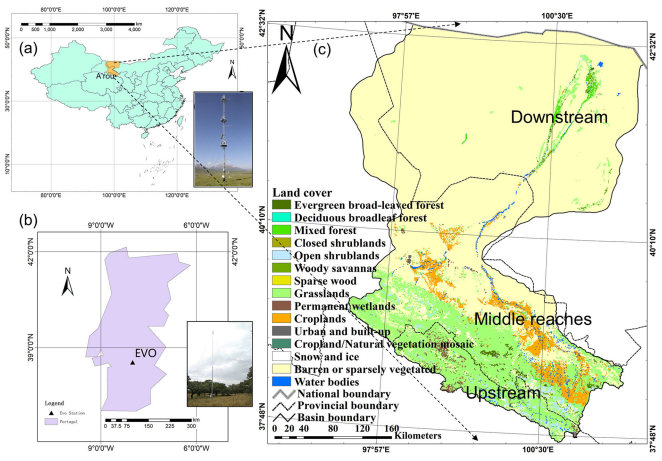

Fig. 1. Study areas and station locations of (a) Arou, China. (b) Evora, Portugal. (c) Displays the Heihe River basin for which the synthetic dataset was generated.

TABLE I
LOCATION AND LAND COVER INFORMATION OF EACH SITE

Site	Latitude Longitude	Elevation	Instrument	Height	Land Cover
AR (A'rou)	38.0565 N, 100.4643 E	3033 m	SI-111	5 m	Grass (alpine meadow)
EVO (Evora)	38.5403 N, 8.0033 W	227 m	KT-15.85 IP	25 m	Woody savannas

C. *LSCT* In-situ *Measurements*

In this article, LSCT measurements for algorithm evaluation were obtained from the Arou, China, and Evora, Portugal sites (see Fig. 1). Detailed location and land cover information for each site is shown in Table I.

1) Arou Station: The Arou site (38.0565 N, 100.4643 E) is located in the Heihe River basin in northwest China. The *in-situ* measurements at Arou were obtained from a meteorological station operated as part of the Heihe Watershed Allied Telemetry Experimental Research (HiWATER) campaign. In HiWATER three key experimental areas (KEAs) were selected to conduct intensive and long-term observations: a cold region experimental area in the mountain cryosphere of the upper reaches, an artificial oasis experimental area in the middle reaches, and a natural oasis experimental area downstream [32]. Arou station (AR) belongs to the cold region experimental area and has an elevation of 3033 m. The underlying canopy of the meteorological station is low grass, and the main vegetation type is alpine meadow. At this station, meteorological parameters such as air temperature, humidity, soil temperature and moisture, wind speed, downward shortwave and longwave radiances, and surface brightness temperatures (BTs) were obtained 5.0 m above the surface. The data used are available online[1] [33]. Soil temperatures measured at 0 cm depth were selected as ground truth values for validating retrieved soil temperature. In many previous studies, retrieved vegetation temperatures were validated using *in-situ* air temperatures, which is considered to be acceptable for dense forest canopies. However, the selected vegetation sites do not meet this criterion. Therefore, ground truth values for validating vegetation temperature were obtained from known surface composition at the station and measured soil temperatures as follows:

$$R'_{v,m} = \frac{R_m - (1-\varepsilon)\cdot R^{\downarrow}_{a,m} - f_s \cdot \varepsilon_s \cdot R'_{s,m}}{f_v \cdot \varepsilon_v} \tag{4}$$

where $R'_{s,m}$ and $R'_{v,m}$ represent the measured thermal radiances of soil and vegetation, respectively; $R^{\downarrow}_{a,m}$ represents the measured downward thermal radiance from the atmosphere; and R_m represents the measured thermal radiance leaving the canopy. Because two Apogee SI-111 TIR radiometers were operated together at AR, their measurements can check each other and were selected to provide BTs for calculating R_m. The uncertainty of SI-111 radiometers was ± 0.2 K over the relevant range. Both radiometers observed the surface at nadir with a spectral range of 8–14 μm and a half-angle field of view of 22°. The target footprint of the radiometers was 12.82 m^2. $R^{\downarrow}_{a,m}$ was obtained from a Kipp & Zonen CNR1 energy balance sensor. Surface BTs and meteorological conditions were automatically measured every 10 min and recorded by a Campbell CR1000 datalogger. The emissivities of the soil and vegetation were set to 0.965 and 0.985, respectively. The pixel emissivity was calculated using an NDVI-based method as mentioned above in (1).

2) Evora Station: Evora (EVO) station (38.5403 N, 8.0033 W) is located approximately 12 km southwest of the town of Evora in the Alentejo region of Portugal. The station was set up in a large area with homogeneous surface cover to minimize complications from spatial scale mismatches between ground-based and satellite sensors. The dominant vegetation types at the station are isolated groups of evergreen cork oak trees and grassland. Several studies of LST product validation have been performed with *in-situ* measurements from this site [34].

EVO uses separate Heitronics KT-15.85 IIP infrared radiometers to measure the relevant surface component temperatures, i.e., the background (grass and ground) and a tree crown, as well as sky radiance at a 53° zenith angle; all measurements are recorded once per minute. The KT-15.85 IIP radiometer has a spectral range of 9.6–11.5 μm and a temperature resolution of 0.03 K with an uncertainty of ± 0.3 K over the relevant range [35]. Temperatures of the ground and tree crown were measured under a view angle of approximately 30°, for which angular emissivity variation of soil and grass can still be regarded as negligible. The target footprint of the radiometers was approximately 14 m^2 with a height of 25 m [36]. The sky radiances measured at a 53° zenith angle were used to estimate downwelling atmospheric radiance [37], [38]. With known component emissivities and after removing the reflected atmospheric radiance from the measured surface radiances, land surface component BTs can be converted to temperatures and be used for validating LSCT results. At EVO, the effective emissivity of ground and tree were set to 0.968 and 0.993, respectively [39].

[1][Online]. Available: http://hiwater.westgis.ac.cn/english/index.asp

According to [34], the surface composition temperature was also calculated using these measured component temperatures. It should be mentioned that because the grass was dry and low there during summer, the measurements for background were used to validate the retrieval results of soil directly.

D. Synthetic Dataset

1) Study Area: Due to the limited availability of suitable *in-situ* measurements, which include LSCT and top-of-canopy observations, a synthetic dataset was used for performing a sensitivity analysis. As a study area, the Heihe River basin was selected [see Fig. 1(c)], which is a typical inland river basin. Because water-stressed ecosystems are massively distributed and easily affected by climate change, studies on LST/LSCT, evapotranspiration estimation, and drought prediction are of high importance and considerable practical value in this study area. As a good area for studying the processes and mechanisms of an eco-hydrological system, several comprehensive remote sensing experiments have been performed in this basin, e.g., the Heihe Basin Field Experiment, Watershed Allied Telemetry Experimental Research and HiWATER [32], [40]–[42]. The study area consists of many typical arid and semi-arid landscapes. In the upstream cold region, the main vegetation types are alpine grassland, alpine meadow, valley bush, and juniper. In the middle stream, the artificial oasis with irrigation from rivers is the main ecosystem, in which corn, wheat, and vegetables are planted. In the downstream Heihe River basin, barren desert or sparsely vegetated surfaces are strongly dominant, whereas, in small areas along the river, there are natural oases with *Populus euphratica* and *Tamarix* canopies.

2) Generation of Top-of-Canopy FVC and BT: The purpose of the sensitivity analysis was to study the relative performance of the combined strategy compared to the multiangle algorithm, while the atmospheric correction procedures remained unchanged. Therefore, in the synthetic dataset, SLSTR data for top-of-canopy FVC and BT were generated instead of generating top-of-atmosphere VNIR and TIR observations and considering data uncertainties by adding errors. Following this approach, the retrieved NDVI maps were used to set the viewing proportion of soil and vegetation in nadir and oblique views. The SLSTR TOC thermal radiances in nadir and oblique views can be generated pixel by pixel using the reference temperatures and the components' visible proportions and emissivities as follows:

$$B_i\left(T_{j,r}\right) = \left(f_{v,j}\varepsilon_v + d\varepsilon\right) B_i\left(T_{v,r}\right) + f_{s,j}\varepsilon_s B_i\left(T_{s,r}\right) \quad j = n, o \tag{5}$$

where $B_i(T_{j,r})$ represents the generated SLSTR thermal radiance; $T_{s,r}$ and $T_{v,r}$ represent the reference temperatures of ground and vegetation, respectively; and B_i represents the Planck function at a channel i, which converts surface temperature to radiance. The LSCT retrieval was performed at 10.85 μm. The subscript j indicates nadir or oblique view. The multiple scattering effect between components was accounted for with the vegetation term ($d\varepsilon$) in (5) according to [43]. It should be mentioned that the LST map of the study area retrieved in nadir view on July 15, 2017, was selected to provide reference temperatures because spatial relationships between neighboring pixels impact the multipixel algorithm. For each pixel, vegetation temperature was assumed to be the reference LST-5 K, and soil temperature was assumed to be the reference LST+5 K. The visible proportions of components were calculated using (2) and (3). Fig. 2(a) and (b) displays the spatial distributions of the reference LST and NDVI maps used in the synthetic dataset, respectively. To avoid the impact from pure pixels, only pixels with FVC values larger than 0.10 and differences in FVC under nadir and oblique views larger than 0.03 were selected for the analysis.

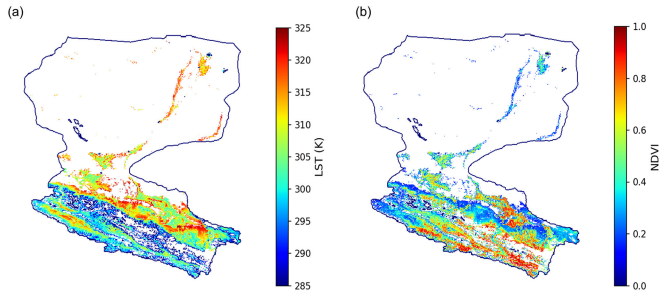

Fig. 2. Spatial distributions of the (a) LST and (b) NDVI on July 15, 2017 in the Heihe River basin.

3) Retrieval Noise: In this study, retrieval noise was categorized into spatial and angular errors. The spatial error was required to account for different spatial resolutions between nadir and oblique views, and only oblique observations had added noise. The TIR radiance ($B_{i,\,e}$) and FVC ($f_{v,o,\,e}$) with spatial errors can be calculated using a weight-averaging method as follows:

$$B_{i,\,e} = \sum_{\xi,\eta} B_i\left(T_{o,r,\xi,\eta}\right) \cdot p_{\xi,\eta} \tag{6}$$

$$f_{v,o,\,e} = e^{-LAI_e \cdot G/u_o} \tag{7}$$

$$\mathrm{LAI}_e = \sum_{\xi,\eta} LAI_{\xi,\eta} \cdot p_{\xi,\eta} \tag{8}$$

where $T_{o,r,\xi,\eta}$ and $\mathrm{LAI}_{\xi,\eta}$ represent the oblique BT and leaf area index (LAI) for a pixel, respectively, with column and row numbers of ξ and η; $p_{\xi,\eta}$ represents the weight of each pixel. According to viewing angles of SLSTR, a 3×3 window was used, and the weights of the center pixel and the surrounding pixel were 1.0 and 0.375, respectively. The LAI for each pixel was retrieved based on an exponential formula from nadir f_s with a homogeneous assumption of pixel leaves [44]. In addition, according to radiative transfer theories, LSCT retrieval would also be affected by uncertainties in atmospheric correction, visible proportions, and component emissivities. Unlike component emissivity, atmospheric correction and FVC are more easily affected by different viewing angles. Therefore, angular errors due to these two factors were included in the sensitivity analysis. The error due to atmospheric correction was considered in top-of-canopy BT. Based on the above considerations, angular errors with a normal distribution were added to the oblique BT (ΔT) and FVC (Δf), and the SLSTR data used in the LSCT

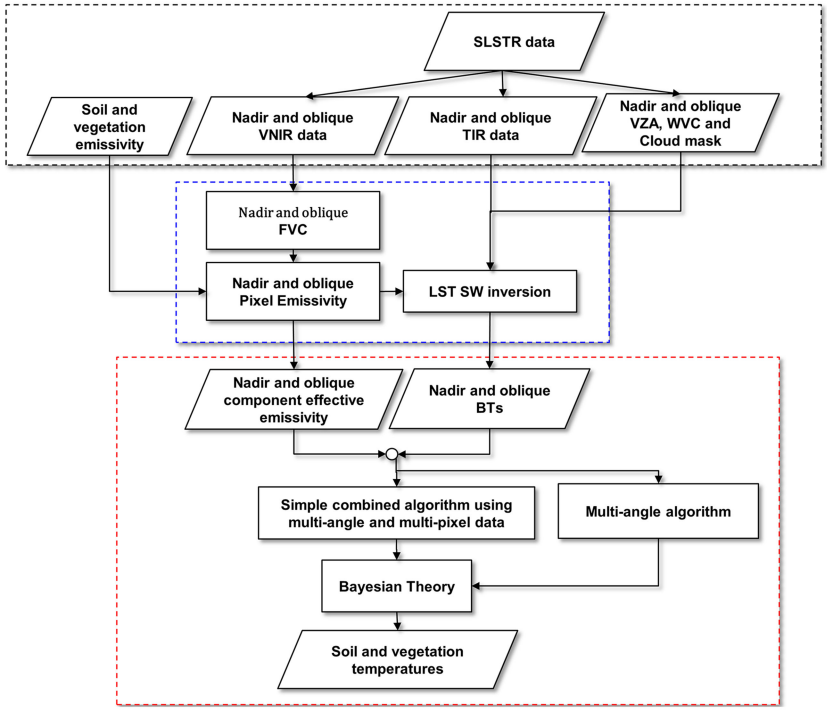

Fig. 3. LSCT retrieval procedure for SLSTR data. Black dotted box: input data. Blue and red boxes: atmospheric correction and LSCT combined retrieval, respectively.

retrieval are calculated as

$$T_{o,r}^{'} = B_{i,e}^{-1} + \Delta T\left(\mu_{BT}, \sigma_{BT}\right) \tag{9}$$

$$f_{o,v}^{'} = f_{o,v,e} + \Delta f\left(\mu_{\mathrm{FVC}}, \sigma_{\mathrm{FVC}}\right) \tag{10}$$

where $T_{j,r}^{'}$ and $f_{j,v}^{'}$ represent the generated BT and FVC, respectively; μ and σ represent the mean and standard deviation, respectively; and $B_{i,e}^{-1}$ represents an inverse process of the Planck function from thermal radiance to BT. According to the uncertainty analysis in [30] and [45], the uncertainties associated with the angular variations in LST retrieval were considered by setting σ_{BT} to 0.25 K and 0.75 K with $\mu_{BT} = 0$. Based on [46], angular errors in FVC were included by setting μ_{FVC} to 0 and σ_{FVC} to 0.03 and 0.09.

III. Method

A. Retrieval Procedure

Fig. 3 illustrates the proposed LSCT retrieval procedure. Before the combined retrieval algorithm (red box) can be performed, an atmospheric correction (blue box) is applied to the TIR input data: this is possible because SLSTR observes the Earth in two thermal channels (8 and 9) under two viewing angles, which allows an LST retrieval performed with SW and dual-angle algorithms. In this study, although LSTs are retrieved, surface actual emissions are used in LSCT retrieval, which are calculated by blackbody emission of a pixel multiplied by its emissivity. Therefore, the LST retrieval process is called atmospheric correction, and the SW algorithm was adopted. The remainder of this section mainly describes the strategy for the algorithm using both multiangle and multipixel observations.

B. Atmospheric Correction

In this study, atmospheric correction was included in the LST retrieval, which was performed in the nadir and oblique views using a generalized SW algorithm proposed in [47] as follows:

$$\mathrm{LST}_j = b_0 + \left(b_1 + b_2\frac{1-\bar{\varepsilon}}{\bar{\varepsilon}} + b_3\frac{\Delta\varepsilon}{\bar{\varepsilon}^2}\right)\frac{T_8+T_9}{2} + \left(b_4 + b_5\frac{1-\bar{\varepsilon}}{\bar{\varepsilon}} + b_6\frac{\Delta\varepsilon}{\bar{\varepsilon}^2}\right)\frac{T_8-T_9}{2} + b_7(T_8-T_9)^2 \tag{11}$$

where $b_0 - b_7$ are the SW coefficients; T_8 and T_9 represent the top-of-atmosphere BTs in SLSTR channels 8 (10.85 μm) and 9 (12.0 μm), respectively; and $\bar{\varepsilon}$ and $\Delta\varepsilon$ are the mean and the differences of emissivity $\varepsilon_{8,j}$ and $\varepsilon_{9,j}$ in SLSTR channels 8 and 9, respectively. In-depth details on the SW algorithm are readily found in the published literature [28], [30], [45], [48]. The SW coefficients were determined by fitting (11) to a synthetic dataset obtained with MODTRAN 5.2 [49] for data from the ASTER spectral library [50] and Seebor V5.2 atmosphere profile library [51]: we used 81 emissivity spectra, including for natural samples of vegetation, water, ice, snow, rock, sand and soil, and 4948 daytime atmospheric profiles to obtain a globally representative data collection. A wide range of surface temperatures was considered, with values varying from T_0-20 K to T_0+4 K at 5 K steps and from T_0-5 K to T_0+29 K at 5 K steps for cold ($T_0 \leq 280$ K) and warm ($T_0 > 280$ K) conditions, respectively,

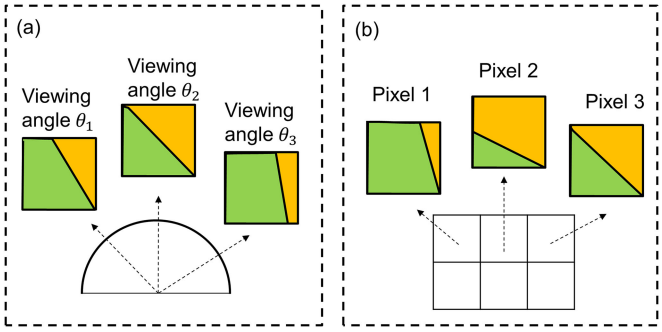

Fig. 4. Observations for (a) multiangle and (b) multipixel algorithms over a vegetation-soil canopy.

where T_0 is the temperature of the lowest layer of the atmospheric profiles. Furthermore, the coefficients were determined for different viewing zenith angles (VZAs) and WVC values: VZAs were 3°, 14.9°, 38.6°, 44.5°, 51.2°, 58°, and 65°, while WVC was subdivided into six classes—i.e., [0, 1.5], [1, 2.5], [2, 3.5], [3, 4.5], [4, 5.5], and [5, 7.8] in units of $\mathrm{g/cm^{-2}}$. Based on illuminating and viewing geometries, the same SW coefficients were used for nadir and oblique view observations. Because the top-of-canopy thermal emissions at nadir and oblique views are required for LSCT retrieval, pixel-average radiances must be multiplied by the corresponding pixel emissivity

$$L_{i,j} = B_i\ (\mathrm{LST}_j) \cdot \varepsilon_{i,j} \tag{12}$$

where $L_{i,j}$ represents the top-of-canopy thermal radiance and subscripts i and j refer to the spectral band and view angle, respectively.

C. LSCT Retrieval

After atmospheric correction, top-of-canopy average thermal radiances of a pixel are obtained in nadir and oblique views. The average thermal radiance ($L_{i,j}$) of a pixel can be expressed in terms of the contributions from its sub-pixel components as follows:

$$L_{i,j} = \sum_{k=1}^{N} f_{j,k}\ \varepsilon_{i,j,k} B_i\ (\mathrm{LST}_k) \tag{13}$$

where LST_k and f_k represent the temperature and visible proportion of component k, respectively; subscript i refers to the spectral band; and subscript j corresponds to the different observations used by the algorithms (see Fig. 4). In a multipixel algorithm, subscript j indexes the different pixels within a window; in a multiangle algorithm, it refers to the observations made over a pixel under different viewing angles. $f_{k,j}\varepsilon_{k,i}$ is the so-called effective emissivity, which represents the contribution of a component to top-of-canopy radiance [52], [53]. It should be mentioned that although multiple scattering effects are not explicitly expressed in (13), the simple estimation used in [30] was adopted for vegetation. In the combined algorithm, LSCT retrieval is performed for the observations in SLSTR channel 8 for each satellite overpass. It should be noted that due to the limited number of observations only average soil and vegetation temperatures can be calculated, regardless of the temperature difference between sunlit and shaded areas.

1) Simple Multiangle and Multipixel Algorithm: Based on (13), the multiangle algorithm can be expressed in matrix form:

$$\overrightarrow{L_a} = \boldsymbol{W} \cdot \overrightarrow{m_a} \tag{14}$$

where $\overrightarrow{L_a}$ is a vector with TIR observations under different viewing angles, $\boldsymbol{W}$ is a matrix containing the components' effective emissivities, and $\overrightarrow{m_a}$ is a vector with the blackbody thermal radiances of the components. The directional emissivity characteristics of each component are described by the column vectors in matrix $\boldsymbol{W}$, while each of its row vectors describes the radiative contribution of the components in a certain viewing direction. Because the visible proportions and emissivity of the components are assumed to be known, the multiangle retrieval procedure can be viewed as a simple linear solution problem. For SLSTR, the number of observations, i.e., nadir or oblique views, at each time is equal to that of component temperatures. Therefore, the blackbody thermal radiances of the components can be retrieved as follows:

$$\overrightarrow{m_a} = \boldsymbol{W}^{-1} \cdot \overrightarrow{L_a}. \tag{15}$$

The multipixel algorithm proposed by Zhan *et al.* [20] was selected for LSCT retrieval, which expresses the spatial distribution of the thermal radiance of a component within a window as a quadratic function of two variables, i.e., the row and column numbers. (13) can then be rewritten as follows:

$$L_{i,j} = \sum_{k=1}^{N} f_{j,k}\ \varepsilon_{i,j,k} \left(a_{k,0} + a_{k,1}\xi_j + a_{k,2}\eta_j + a_{k,3}\xi_j^2 + a_{k,4}\eta_j^2 + a_{k,5}\xi_j\eta_j\right) \tag{16}$$

where $a_{k,0}$-$a_{k,5}$ are unknown coefficients for component k in the multipixel algorithm; ξ_j and η_j are the column and row numbers of pixel j, respectively; and N is the number of components. A set of TIR observation equations in the selected window can also be rewritten in matrix form

$$\overrightarrow{L_p} = \boldsymbol{H} \cdot \vec{X} \tag{17}$$

where $\overrightarrow{L_p}$ is the vector of TIR observations of different pixels, $\boldsymbol{H}$ is a matrix of coefficients associated with ξ_j and η_j, and $\vec{X}$ is a vector containing the unknown coefficients ($a_{k,0}$-$a_{k,5}$). Because the visible proportions and emissivity of components are assumed to be known, the set of (17) can be solved when the number of available pixels in the selected window is larger than the number of unknown coefficients (6×N). Once the coefficients are obtained, the thermal radiance of each component k can be calculated using weighted averaging with a Gaussian function as follows:

$$m_{p,\,k} = \sum_{j=1}^{M} F_{j,n}\ \left(a_{k,0} + a_{k,1}\xi_j + a_{k,2}\eta_j + a_{k,3}\xi_j^2 + a_{k,4}\eta_j^2 + a_{k,5}\xi_j\eta_j\right) \tag{18}$$

$$F_j = \frac{1}{2\pi\sigma^2} e^{-\left({\xi_j}^2+{\eta_j}^2\right)/2\sigma^2} \tag{19}$$

where M represents the number of pixels in a selected window. It should be mentioned that the weight coefficients ($F_{k,n}$) calculated by the Gaussian function were normalized.

Following [23] and [24], the multiangle LSCT retrieval can be performed for each pixel. Following [20], LSCT can be retrieved from multipixel observations in nadir view. In this study, the multipixel observations in both nadir and oblique views were used in (17), which enables a multiangle retrieval under an assumption using a quadratic function for multipixel information. In this study, a 5×5 window was selected for retrieving coefficients $\vec{X}$ by using a least-squares method: usually, this provides enough equations when only soil and vegetation components are considered.

2) Bayesian Combination Strategy: In the above simple combined algorithm, the multiangle retrieval was performed using observations in a window. The retrieved result for a pixel would inevitably be affected by surrounding pixels. To reduce this effect, a multiangle retrieval was performed again using observations from a pixel, and a Bayesian strategy was adopted to combine retrieved results from a window and a pixel. The maximal posterior probability of the blackbody thermal radiance of components can then be calculated with (20), where the sensor noise and component radiance are assumed to have a Gaussian distribution.

$$\vec{m} = \left(\boldsymbol{W}^{\boldsymbol{T}}\boldsymbol{C}_{\boldsymbol{D}}^{-1}\boldsymbol{W} + \boldsymbol{C}_{\boldsymbol{M}}^{-1}\right)^{-1}\left(\boldsymbol{W}^{\boldsymbol{T}}\boldsymbol{C}_{\boldsymbol{D}}^{-1}\overrightarrow{L_a} + \boldsymbol{C}_{\boldsymbol{M}}^{-1}\overrightarrow{m_p}\right) \tag{20}$$

where $\vec{m}$ is a vector containing the results of the Bayesian combined algorithm; $\boldsymbol{C_D}$ is the covariance matrix associated with measured and modeled observations; $\boldsymbol{C_M}$ is the covariance matrix associated with measured and a priori thermal radiances of the components [12]; $\overrightarrow{m_p}$ is the vector containing the components' thermal radiances as determined with the simple combined algorithm; and $\overrightarrow{L_a}$ and $\boldsymbol{W}$ have the same meaning as in the multiangle algorithm described above. In this study, the Bayesian strategy determines the weights of a priori information $\overrightarrow{m_p}$ and multiangle information from a pixel to result $\vec{m}$, and the determination criteria are mainly based on the intensity of the pixel angular effect. When the pixel angular effect is weak, the reliability of retrieval results from $\overrightarrow{L_a}$ is reduced, and the result $\vec{m}$ is mainly determined by $\overrightarrow{m_p}$.

IV. Results

A. Sensitivity Analysis for Synthetic Data

The various input data are associated with a certain uncertainty. Therefore, the effect of this uncertainty on the proposed LSCT retrieval algorithm must be analyzed. Because LSCT *in-situ* data are scarce, a synthetic dataset for the Heihe River basin was used to conduct a sensitivity analysis. The effects due to different spatial and angular errors were analyzed. The evaluation results under different vegetation types and FVC differences were also provided. In this sensitivity analysis, results retrieved by the multiangle, simple and Bayesian combined algorithms were compared.

1) Evaluations Results for Different Retrieval Errors: Fig. 5 displays the evaluation results for three algorithms when different spatial and angular errors were added. In Fig. 5(a) and (b), the retrieved results were affected only by different spatial resolutions between nadir and oblique views. Such spatial errors can reach 4.5 K, and as they increased, the retrieval performance for multiangle algorithm significantly decreased with root mean squared errors (RMSEs) larger than 10.0 K. The simple combined algorithm performed better, whereas large RMSEs also appeared, particularly for T_s, which induced the effect from surrounding pixels in a multipixel algorithm. In a simple combined algorithm, the difference in RMSEs between T_s and T_v can be explained by the fact that T_s can be significantly affected by varying FVCs because of the large temperature difference between its sunlit and shaded areas. In Fig. 5(c)–(f), angular errors in BTs and FVCs increased, and RMSEs for three algorithms increased, particularly for cases with low spatial errors. In Fig. 5(c)–(f), RMSEs for cases with large spatial errors were slightly lower than those in Fig. 5(a) and (b), which can be attributed to less data in these cases and unstable retrieved results. Table II displays the total RMSEs for T_s and T_v in Fig. 5. As the spatial errors increased, the RMSE for T_s increased from 1.22 to 1.70 K, and that for T_v increased from 1.95 to 3.06 K. Among these algorithms, the Bayesian combined algorithm performed best. By comparing the results between multiangle and simple combined algorithms, the multipixel information can be found useful to reduce the effect due to different spatial resolutions between nadir and oblique views. By comparing the results between simple and Bayesian combined algorithms, the result retrieved from multiangle observations for a pixel can improve the result, whereas its function weakened as angular errors increased.

2) Evaluation for Different Vegetation Types: Several complex and diverse ecosystems exist in the study area. Therefore, LSCTs retrieved for different vegetation types were provided in Fig. 6(a) and (b). The study area was classified into five main land cover types: grassland, cropland, sparse forest, barren or sparsely vegetated, and other. No angular errors of BT and FVC were introduced. Similar RMSE trends were found for three retrieval algorithms regardless of vegetation types. Slight differences were found between cropland and barren types. Compared to the other four types, the RMSEs of cropland were slightly higher and lower for T_s and T_v, respectively. In contrast, the RMSEs for barren land were slightly lower and higher for T_s and T_v, respectively. This phenomenon can be attributed to the different canopy structures of these types. In this context, a further analysis was performed to link the evaluation results to FVC [see Fig. 6(c) and (d)]. As FVC increased, the RMSEs for T_s and T_v increased and decreased, respectively. The difference in RMSE between cropland and barren types can be explained by the fact that their FVCs were 0.55 and 0.31, respectively. In addition, by comparing the three algorithms, the RMSEs of the multiangle algorithm sharply varied with FVC.

3) Evaluation for Different FVC Differences: In addition to FVC, the evaluation results of LSCT, particularly for the multiangle algorithm, would also be affected by FVC difference according to analysis in [23] and [24]. Fig. 7 displays the evaluation

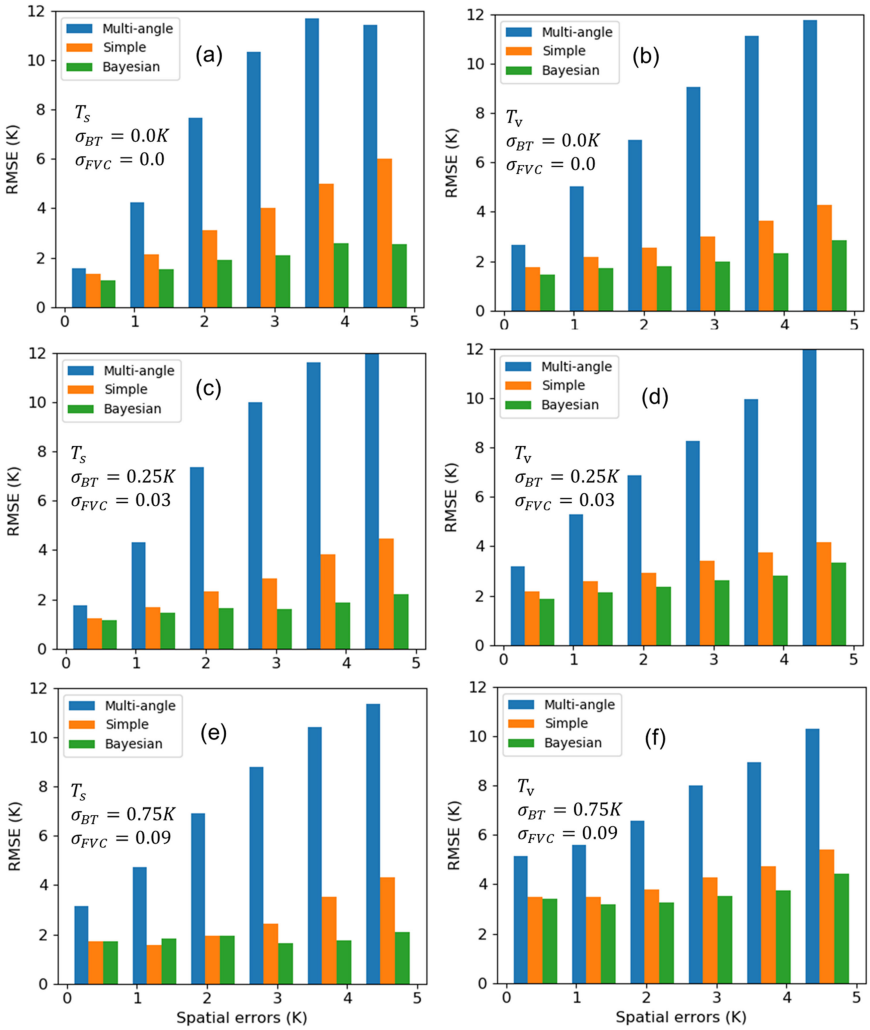

Fig. 5. LSCTs retrieved by the multiangle, simple and Bayesian combined algorithms with spatial error due to different spatial resolutions. (a) and (b) correspond to induced errors with $\sigma_{BT} = 0.0$ K and $\sigma_{\mathrm{FVC}} = 0.0$. (c) and (d) correspond to induced errors with $\sigma_{BT} = 0.25$K and $\sigma_{\mathrm{FVC}} = 0.03$. (e) and (f) correspond to induced errors with $\sigma_{BT} = 0.75$K and $\sigma_{\mathrm{FVC}} = 0.09$.

TABLE II
STATISTICAL INFORMATION FOR THREE RETRIEVAL ALGORITHMS UNDER DIFFERENT RETRIEVAL ERRORS

	$\sigma_{BT} = 0.0K, \sigma_{FVC} = 0.0$	$\sigma_{BT} = 0.25K, \sigma_{FVC} = 0.03$	$\sigma_{BT} = 0.75K, \sigma_{FVC} = 0.09$
$T_{s,ma}$ (K)	3.34	3.91	4.16
$T_{s,simple}$ (K)	1.72	1.67	2.14
$T_{s,Bayesain}$ (K)	1.22	1.23	1.70
$T_{v,ma}$ (K)	4.25	5.29	5.72
$T_{v,simple}$ (K)	2.49	2.44	3.24
$T_{v,Bayesain}$ (K)	1.95	2.03	3.06

results for three algorithms with FVC difference. As the FVC difference increased, the RMSEs for retrieved results for the multiangle algorithm decreased. Because of the large spatial effects, the decline was not significant. The RMSEs for the simple combined algorithm slightly varied and increased in some cases. It should be mentioned that as the FVC difference increased, the increasing difference in RMSE between simple and Bayesian combined algorithms benefitted from the improvement of the multiangle algorithm. In addition, according to Bayesian theory, the weight of the pixel multiangle algorithm also increased. However, as angular errors increased, the difference between simple and Bayesian combined algorithms decreased.

B. *LSCT Validation Based on* In-situ *Measurements*

In this article, LSCTs retrieved from SLSTR data were validated against *in-situ* measurements from TIR radiometers. The RMSEs of LSCT results retrieved by the combined algorithm

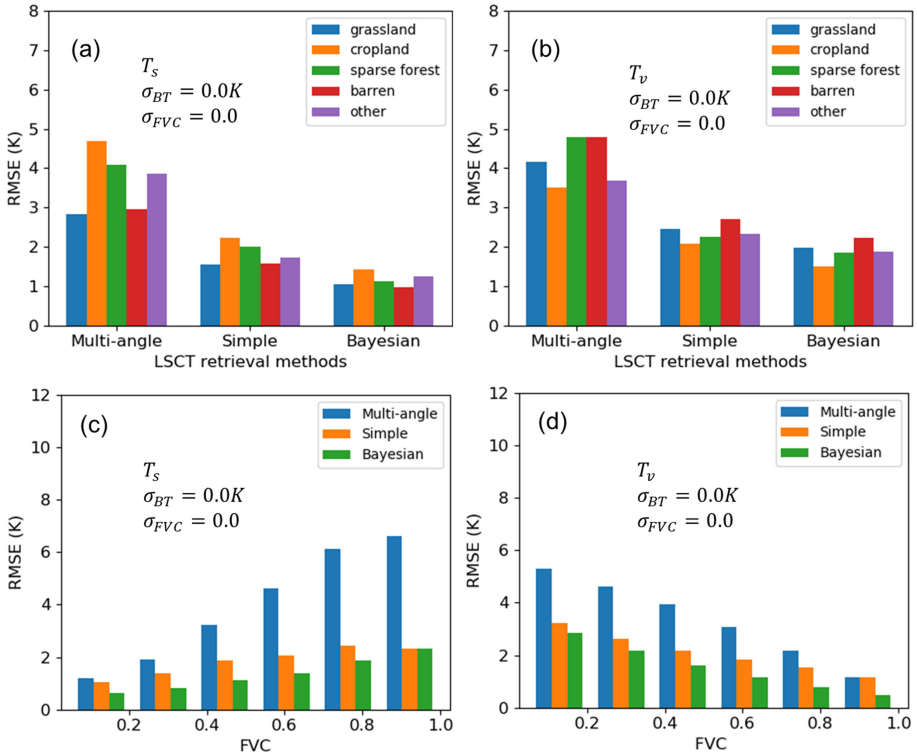

Fig. 6. (a) and (b) correspond to T_s and T_v RMSEs of the three algorithms for different vegetation types. (c) and (d) correspond to T_s and T_v RMSE of the three algorithms with FVC.

were found to be lower than approximately 3.0 K according to sensitivity analysis. In addition to removing cloud-contaminated data, data with differences between retrieved and *in situ* LSCTs larger than 9.0 K were removed based on 3-sigma criteria [28]. Fig. 8(a) and (b) displays the *in-situ* measured and retrieved component and pixel-average temperatures at the AR and EVO sites, respectively. The red/blue belts represent temperature differences between the weighted average and individual soil/vegetation components. Because of the different climates, the temperatures at the AR site decreased considerably during the observation period, whereas those at the EVO site increased slightly. At both sites, the change in component temperatures and pixel-average temperatures was consistent, and soil temperatures were significantly larger than vegetation temperatures. Most temperature differences between soil and vegetation were less than 10 K at the AR site, whereas they reached 20 K at the EVO site. This difference may be explained by the fact that the vegetation component at the EVO site consists of tree crowns, whereas the vegetation component at the AR site consists of grass.

Fig. 9(a) and (d) shows *in-situ* LSCTs versus LSCTs retrieved with the combined algorithm for sites AR and EVO, respectively. At AR, the RMSE for T_v was lower than that for T_s, with values of 1.91 K and 3.09 K, respectively. The strong overestimation of T_s (bias of 1.68 K) is mainly due to several points at high temperatures. The RMSEs for T_s and T_v at the EVO site were 3.71 K and 3.42 K, respectively, and slightly larger than those at the AR site. There were some underestimations and overestimations for T_s and T_v, respectively, with corresponding bias values of -1.83 K and 1.64 K. The results retrieved by the multiangle and simple combined algorithms at these two sites are also shown in Fig. 9(b), (c), (e), and (f). The RMSEs for the multiangle and simple combined algorithms were larger than that for the Bayesian combined algorithm. At the AR site, the T_s and T_v RMSEs of the multiangle algorithm were 3.50 K and 1.94 K, respectively, whereas the corresponding values at the EVO site were 3.71 K and 3.75 K, respectively. For the simple combined algorithm, the T_s and T_v RMSEs at the AR site were 3.89 K and 2.45 K, respectively, while the corresponding values at the EVO site were 3.83 K and 3.62 K, respectively. The coefficient of determination (R^2) for the Bayesian combined algorithm was larger than the corresponding values for the multiangle and simple combined algorithms. Furthermore, fewer of the results retrieved with the multiangle and simple combined algorithms satisfied the threshold condition ($<$9 K) than for the Bayesian combined algorithm: at the AR and EVO sites, the number of valid data points for the Bayesian combined algorithm was 38, whereas it was 28 and 36 for the multiangle and simple combined algorithms, respectively. The generally low number of data points may also partially explain the relatively small differences in performance between algorithms.

V. Discussion

A. Evaluation Problems

Recently, LSCT retrievals have attracted more attention because more detailed subpixel temperature information is required by many applications. Previous studies usually performed

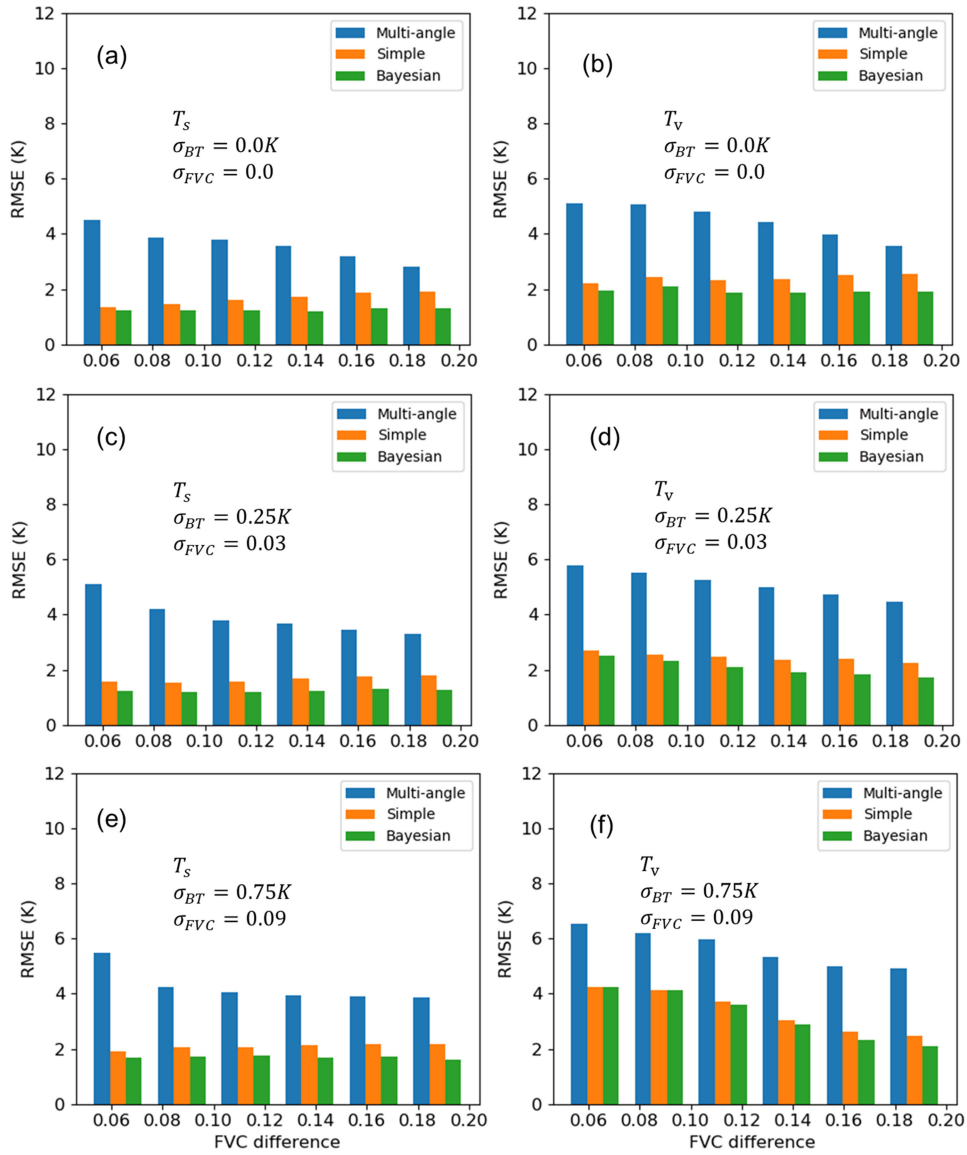

Fig. 7. LSCTs retrieved by the multiangle, simple and Bayesian combined algorithms with FVC difference between nadir and oblique views. (a) and (b) correspond to cases without angular errors, (c) and (d) correspond to induced errors with $\sigma_{BT} = 0.25$K and $\sigma_{\mathrm{FVC}} = 0.03$, and (e) and (f) correspond to induced errors with $\sigma_{BT} = 0.75$K and $\sigma_{\mathrm{FVC}} = 0.09$.

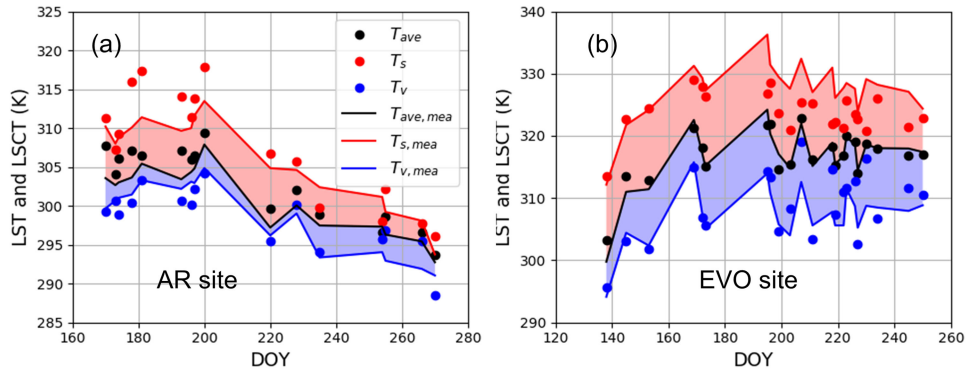

Fig. 8. Temporal variation of measured and retrieved surface temperatures at (a) AR and (b) EVO.

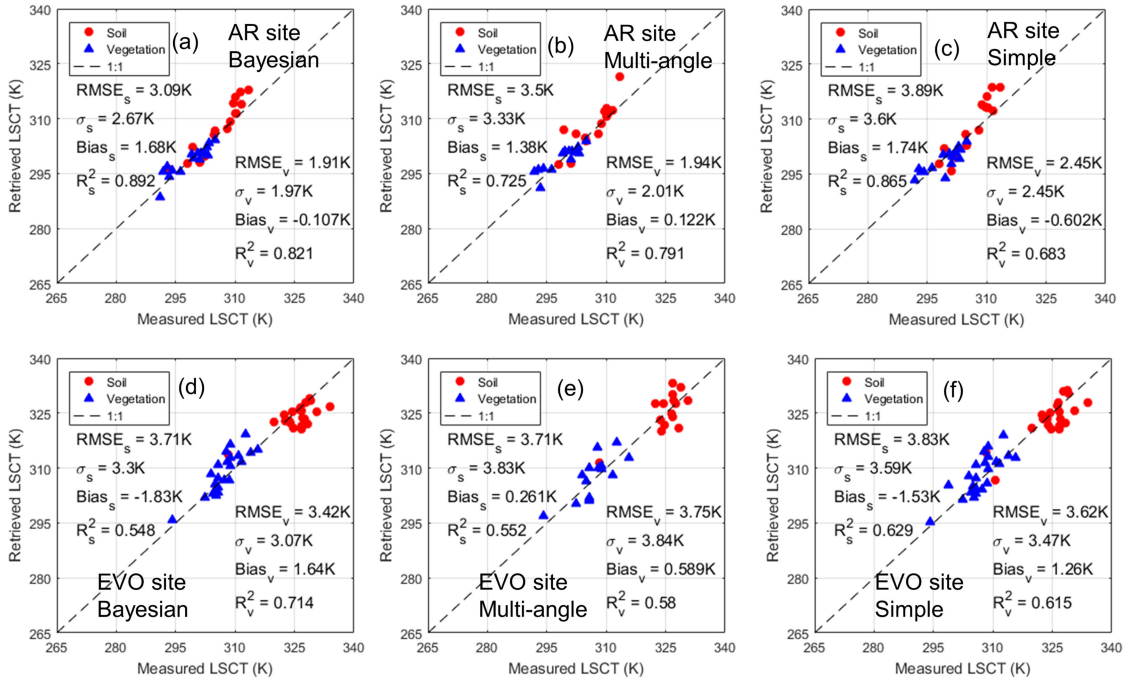

Fig. 9. *In-situ* LSCT versus retrieved LSCT at sites (a)–(c) AR and (d)–(f) EVO. The presented LSCTs were retrieved with the (a), (d) Bayesian combined, (b), (e) multiangle, and (c), (f) simple combined algorithms using SLSTR data from DOY 120 to 270 in 2017.

LSCT retrieval with an individual algorithm, which frequently caused large discrepancies in the retrieved results. In this study, a simple combined algorithm was proposed to together use multipixel and multiangle observations in a window, and then the result retrieved from multiangle observation for a pixel was introduced by a Bayesian strategy. The results indicate that the Bayesian combined algorithm has a more robust performance relative to the multiangle algorithm and simple combined algorithm, since it utilizes more available data to reduce RMSE. Nevertheless, the evaluation and validation of the retrieval algorithms were limited by the availability of *in situ* measurements: future validation work would greatly benefit from additional *in situ* LSCTs. Another limitation is linked to the use of a synthetic dataset. Because of the lack of uncertainty information on the *in situ* LSCT, we assumed a combination of spatial and angular errors based on typical uncertainties in previous studies. Furthermore, we ignored the directional anisotropy of soil emissivity, since this kind of information for a component is generally not used in LST and LSCT retrieval algorithms. However, a non-negligible directional anisotropy of soil emissivity has been reported in [54]–[56], which would lower the BTs for SLSTR's oblique view. To investigate this concern, we used an empirical model of soil emissivity for generating synthetic SLSTR BTs as follows [57]:

$$\varepsilon_{s,o}\ (\theta_v) = \varepsilon_{s,n}\ - 8.7 \times 10^{-9}\ \times \theta_v^{\alpha} \tag{21}$$

where $\varepsilon_{s,n}$ and $\varepsilon_{s,o}(\theta_v)$ represent soil emissivity at nadir and at VZA θ_v (degree), respectively, and α is a parameter describing the dependency of soil emissivity on the viewing angle, which here was set to 3.3. When $\varepsilon_{s,n}$= 0.955, from nadir to oblique 55° views, soil emissivity decreased to 0.950. The evaluation results are shown in Fig. 10, where no angular errors were added. Compared with the results in Fig. 6(c) and (d), the RMSEs for three algorithms all increased in Fig. 10(a) and (b), particularly for the case with low FVC. However, although all results deteriorated, the Bayesian combined algorithm still performed best. It should be mentioned that the directional anisotropy of soil emissivity would also affect LST retrieval, and an underestimation of soil emissivity may result in an overestimation of LST. Because surface BTs were used in LSCT retrieval, which was calculated by pixel-average blackbody emission multiplied by the corresponding emissivity as shown in (12), the overestimation of LST would be corrected to some extent. Therefore, its effect was not addressed in this article.

B. Limitations and Future Improvements of the Combination Algorithm

A possible reason for large LSCT RMSEs in valuation was that the RMSEs for nadir LSTs were 2.11 K and 1.81 K, respectively, corresponding to AR and EVO sites. According to [30], the retrieval accuracy for oblique LSTs may be worse. Moreover, the retrieval results of LSCT would also be affected by the uncertainties of other inputs. The original aim for the combined algorithm was to avoid the disadvantage of the multiangle algorithm due to different spatial resolution between nadir and oblique views. In addition to LST retrieval, the proposed combined algorithms would also be affected by individual multipixel and multiangle algorithms. Here, we provide a brief overview of some disadvantages of the individual algorithms.

1) For a multiangle algorithm, in addition to FVC, directional anisotropy is an important factor [23], [24]. Large RMSEs for

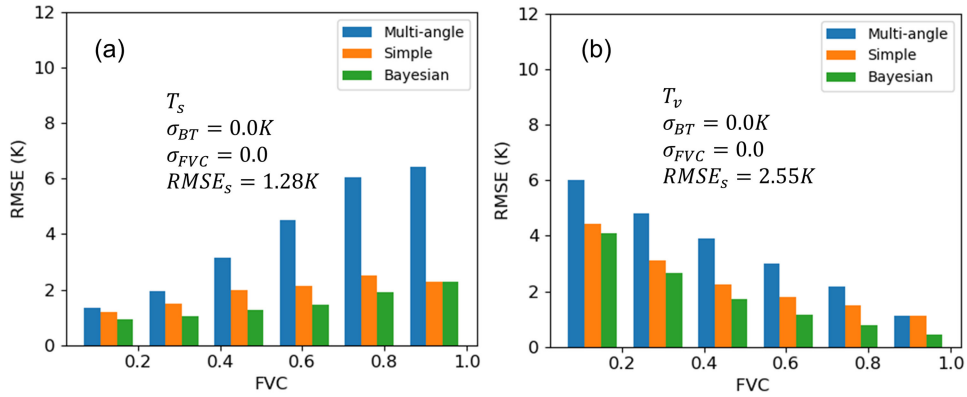

Fig. 10. RMSEs of three algorithms with FVC for (a) T_s and (b) T_v with directional anisotropy of soil emissivity.

the multiangle algorithm were mainly observed for pixels with FVC differences between nadir and oblique views lower than 0.10, which occurred over homogeneous canopies with LAIs lower than 0.5 or greater than 4.0. When only pixels with FVC differences larger than 0.10 were considered, the corresponding values decreased to 1.06 K and 1.37 K.

2) The multipixel algorithm performed worse than in [20], which can be attributed to the retrieval accuracy of SLSTR's LST.

3) The multiangle and multipixel algorithms assume that temperature differences are mainly related to land cover differences, i.e., soil and vegetation. However, this assumption does not hold if there are sunlit and shaded areas. The situation becomes even more complex in mountainous areas, which usually exhibit temperature differences with altitude and between sunlit and shaded areas due to hill shadows. If only the temperature difference between the average soil and vegetation is assumed, LSCT retrieval discrepancies are inevitable in all such cases.

Nevertheless, the combined algorithm using both multiangle and multipixel observations displayed robust performance and, therefore, is a good option for actual retrieval tasks. While we focused on the combination of multiple algorithms, the combined algorithm would benefit from future improvements of the individual algorithms and LST retrieval. Considering the different weaknesses of the individual algorithms, more detailed knowledge of their performance could be used to improve their combination. This can be achieved with comparisons and evaluations based on more comprehensive *in-situ* experiments. For a more comprehensive investigation of combining algorithms and data sources, other strategies, e.g., Bayesian model averaging, support vector machines and artificial neural networks—are also worth exploring for LSCT retrieval [58].

VI. Conclusion

LSCT retrieval methods aim at providing more detailed information on LST, particularly over heterogeneous surfaces. Several studies reported that such methods are useful for various applications, e.g., evapotranspiration estimation and vegetation monitoring. Based on different types of TIR observations, a variety of LSCT retrieval algorithms have been proposed, and their strengths and weaknesses investigated. In the last decade, the use of methods involving the fusion of multisensor data and multiple algorithms has increased. The study presented here is the first attempt to use multiangle and multipixel observations in a robust LSCT retrieval method. According to an analysis based on synthetic data, the simple combined algorithm can significantly reduce the effect from spatial errors in oblique view by using multipixel and multiangle information in a window, and the Bayesian combined algorithm can further improve LSCT results by introducing retrieved results from multiangle information of a pixel. For *in-situ* measurements from grass and sparse forest sites, the Bayesian combined algorithm retrieved more LSCTs with lower RMSEs than other algorithms: the RMSEs of the Bayesian combined algorithm were 3.09 K and 1.91 K for T_s and T_v at the grass site, respectively, and 3.71 K and 3.42 K at the sparse forest site, respectively. Considering that temperature differences between soil and vegetation components can reach 20 K, the retrieved LSCTs add valuable information to pixel-average LSTs. When algorithms of LST retrieval and individual LSCT retrieval are developed, the LSCT retrieved results by the combined algorithm would also be improved.

References

[1] Z.-L. Li *et al.*, "Land surface emissivity retrieval from satellite data," *Int. J. Remote Sens.*, vol. 34, pp. 3084–3127, 2013.

[2] J. M. Norman, W. P. Kustas, and K. S. Humes, "Source approach for estimating soil and vegetation energy fluxes in observations of directional radiometric surface temperature," *Agricultural Forest Meteorol.*, vol. 77, pp. 263–293, 1995.

[3] T. Hu *et al.*, "Monitoring agricultural drought in Australia using MTSAT-2 land surface temperature retrievals," *Remote Sens. Environ.*, vol. 236, 2020, Art. no. 111419.

[4] J. C. Jiménez-Muñoz, J. Cristóbal, J. A. Sobrino, G. Sòria, M. Ninyerola, and X. Pons, "Revision of the single-channel algorithm for land surface temperature retrieval from Landsat thermal-infrared data," *IEEE Trans. Geosci. Remote Sens.*, vol. 47, no. 1, pp. 339–349, Jan. 2009.

[5] Z. Wan and J. Dozier, "A generalized split-window algorithm for retrieving land-surface temperature from space," *IEEE Trans. Geosci. Remote Sens.*, vol. 34, no. 4, pp. 892–905, Jul. 1996.

[6] Z. Wan and Z.-L. Li, "A physics-based algorithm for retrieving land-surface emissivity and temperature from EOS/MODIS data," *IEEE Trans. Geosci. Remote Sens.*, vol. 35, no. 4, pp. 980–996, Jul. 1997.

[7] A. Gillespie, S. Rokugawa, T. Matsunaga, J. S. Cothern, S. Hook, and A. B. Kahle, "A temperature and emissivity separation algorithm for Advanced Spaceborne Thermal Emission and Reflection Radiometer (ASTER) images," *IEEE Trans. Geosci. Remote Sens.*, vol. 36, no. 4, pp. 1113–1126, Jul. 1998.

[8] G. C. Hulley and S. J. Hook, "Generating consistent land surface temperature and emissivity products between ASTER and MODIS data for earth science research," *IEEE Trans. Geosci. Remote Sens.*, vol. 49, no. 4, pp. 1304–1315, Apr. 2011.

[9] L. Song *et al.*, "Estimation of surface heat fluxes using multi-angular observations of radiative surface temperature," *Remote Sens. Environ.*, vol. 239, 2020, Art. no. 111674.

[10] W. Zhu, S. Jia, and A. Lv, "A time domain solution of the modified temperature vegetation dryness index (MTVDI) for continuous soil moisture monitoring," *Remote Sens. Environ.*, vol. 200, pp. 1–17, 2017.

[11] S. Park, D. Ryu, S. Fuentes, H. Chung, E. Hernández-Montes, and M. O'Connell, "Adaptive estimation of crop water stress in nectarine and peach orchards using high-resolution imagery from an unmanned aerial vehicle (UAV)," *Remote Sens.*, vol. 9, 2017, Art. no. 828.

[12] J. Timmermans, W. Verhoef, V. D. C. Tol, and Z. Su, "Retrieval of canopy component temperatures through Bayesian inversion of directional thermal measurements," *Hydrol. Earth Syst. Sci.*, vol. 13, pp. 1249–1260, 2009.

[13] Z. Bian *et al.*, "A semi-empirical approach for modeling the vegetation thermal infrared directional anisotropy of canopies based on using vegetation indices," *ISPRS J. Photogramm. Remote Sens.*, vol. 160, pp. 136–148, 2020.

[14] B. Cao *et al.*, "A review of earth surface thermal radiation directionality observing and modeling: Historical development, current status and perspectives," *Remote Sens. Environ.*, vol. 232, 2019, Art. no. 111304.

[15] Z. Bian, Q. Xiao, B. Cao, Y. Du, H. Li, and H. Wang, "Retrieval of leaf, sunlit soil, and shaded soil component temperatures using airborne thermal infrared multiangle observations," *IEEE Trans. Geosci. Remote Sens.*, vol. 54, no. 8, pp. 4660–4671, Aug. 2016.

[16] Z. Bian *et al.*, "An analytical four-component directional brightness temperature model for crop and forest canopies," *Remote Sens. Environ.*, vol. 209, pp. 731–746, 2018.

[17] Z. Bian *et al.*, "The effects of tree trunks on the directional emissivity and brightness temperatures of a leaf-off forest using a geometric optical model," *IEEE Trans. Geosci. Remote Sens.*, to be published, doi: 10.1109/TGRS.2020.3011157.

[18] W. Zhan *et al.*, "Disaggregation of remotely sensed land surface temperature: Literature survey, taxonomy, issues, and caveats," *Remote Sens. Environ.*, vol. 131, pp. 119–139, 2013.

[19] K. Sun and S.-B. Chen, "Genetic algorithm based surface component temperatures retrieval by integrating MODIS TIR DATA from Terra and Aqua satellites," *J. Infrared Millimeter Waves*, vol. 31, pp. 462–468, 2012.

[20] W. Zhan, Y. Chen, J. Zhou, and J. Li, "An algorithm for separating soil and vegetation temperatures with sensors featuring a single thermal channel," *IEEE Trans. Geosci. Remote Sens.*, vol. 49, pp. 1796–1809, 2011.

[21] Z. Wei, A. Li, J. Bian, H. Jin, and Z. Zhang, "A synergetic algorithm for mid-morning land surface soil and vegetation temperatures estimation using MSG-SEVIRI products and TERRA-MODIS products," *Remote Sens.*, vol. 6, pp. 2213–2238, 2014.

[22] M. Menent *et al.*, "Estimation of soil and vegetation temperatures with multiangular thermal infrared observations: IMGRASS, HEIFE, and SGP 1997 experiments," *J. Geophys. Res., Atmospheres*, vol. 106, pp. 11997–12010, 2001.

[23] Z. Li, M. Stoll, Z. Renhua, J. Li, and S. Zhongbo, "On the separate retrieval of soil and vegetation temperatures from ATSR data," *Sci. China Ser. D, Earth Sci.*, vol. 44, pp. 97–111, 2001.

[24] L. Jia, Z. l. Li, M. Menenti, Z. Su, W. Verhoef, and Z. Wan, "A practical algorithm to infer soil and foliage component temperatures from bi-angular ATSR-2 data," *Int. J. Remote Sens.*, vol. 24, pp. 4739–4760, 2003.

[25] J. Yang and L. Jia, "Retrieval of soil and vegetation component temperatures based on dual-angular AATSR remote sensing data," *Remote Sens. Technol. Appl.*, vol. 29, pp. 247–257, 2014.

[26] C. Donlon *et al.*, "The global monitoring for environment and security (GMES) Sentinel-3 mission," *Remote Sens. Environ.*, vol. 120, pp. 37–57, 2012.

[27] X. Hu *et al.*, "Agricultural drought monitoring using European Space Agency Sentinel 3A land surface temperature and normalized difference vegetation index imageries," *Agricultural Forest Meteorol.*, vol. 279, 2019, Art. no. 107707.

[28] J. Sobrino *et al.*, "Synergistic use of MERIS and AATSR as a proxy for estimating Land Surface Temperature from Sentinel-3 data," *Remote Sens. Environ.*, vol. 179, pp. 149–161, 2016.

[29] C. Henocq *et al.*, "OLCI/SLSTR SYN L2 Algorithm and Products Overview," in *Proc. IEEE Int. Geosci. Remote Sens. Symp.*, 2018, pp. 8723–8726.

[30] H. Li *et al.*, "Comparison of the MuSyQ and MODIS collection 6 land surface temperature products over barren surfaces in the Heihe River Basin, China," *IEEE Trans. Geosci. Remote Sens.*, vol. 57, no. 10, pp. 8081–8094, Oct. 2019.

[31] G. C. Hulley, S. J. Hook, E. Abbott, N. Malakar, T. Islam, and M. Abrams, "The ASTER global emissivity dataset (ASTER GED): Mapping Earth's emissivity at 100 meter spatial scale," *Geophys. Res. Lett.*, vol. 42, pp. 7966–7976, 2015.

[32] X. Li *et al.*, "Heihe watershed allied telemetry experimental research (HiWATER): Scientific objectives and experimental design," *Bull. Amer. Meteorol. Soc.*, vol. 94, pp. 1145–1160, 2013.

[33] Z. Xu *et al.*, "Intercomparison of surface energy flux measurement systems used during the HiWATER-MUSOEXE," *J. Geophys. Res., Atmospheres*, vol. 118, pp. 13140–13157, 2013.

[34] S.-B. Duan *et al.*, "Validation of Collection 6 MODIS land surface temperature product using *in situ* measurements," *Remote Sens. Environ.*, vol. 225, pp. 16–29, 2019.

[35] E. Theocharous *et al.*, "The 2016 CEOS infrared radiometer comparison: Part II: Laboratory comparison of radiation thermometers," *J. Atmos. Ocean. Technol.*, vol. 36, pp. 1079–1092, 2019.

[36] P. Guillevic *et al.*, "Land surface temperature product validation best practice protocol. Version 1.1, Best practice for satellite-derived land product validation," P. Guillevic, F. Göttsche, J. Nickeson, and M. Román, Eds. Land Product Validation Subgroup (WGCV / CEOS), Washington, DC, USA, p. 58, 2018.

[37] G. C. Hulley and S. J. Hook, "Generating consistent land surface temperature and emissivity products between ASTER and MODIS data for earth science research," *IEEE Trans. Geosci. Remote Sens.*, vol. 49, pp. 1304–1315, 2011.

[38] A. Tarantola, *Inverse Problem Theory and Methods for Model Parameter Estimation*. Philadelphia, PA, USA: SIAM, 2005.

[39] S. L. Ermida, I. F. Trigo, C. C. Dacamara, F. M. Göttsche, F. S. Olesen, and G. Hulley, "Validation of remotely sensed surface temperature over an oak woodland landscape – The problem of viewing and illumination geometries," *Remote Sens. Environ.*, vol. 148, pp. 16–27, 2014.

[40] Y. Hu and Y. Gao, "Some new understandings of processes at the land surface in arid area from the HEIFE," *Acta Meteorologica Sinica*, vol. 52, pp. 285–296, 1994.

[41] X. Li *et al.*, "Watershed allied telemetry experimental research," *J. Geophys. Res., Atmospheres*, vol. 114, pp. 1–19, 2009.

[42] L. Song *et al.*, "Application of remote sensing-based two-source energy balance model for mapping field surface fluxes with composite and component surface temperatures," *Agricultural Forest Meteorol.*, vol. 230, pp. 8–19, 2016.

[43] C. Francois, "The potential of directional radiometric temperatures for monitoring soil and leaf temperature and soil moisture status," *Remote Sens. Environ.*, vol. 80, pp. 122–133, 2002.

[44] R. B. Myneni and J. Ross, *Photon-Vegetation Interactions: Applications in Optical Remote Sensing and Plant Ecology*. Berlin, Germany: Springer, 2012.

[45] S. Zhang *et al.*, "Improvement of split-window algorithm for land surface temperature retrieval from Sentinel-3A SLSTR data over barren surfaces using ASTER GED product," *Remote Sens.*, vol. 11, 2019, Art. no. 3025.

[46] J. R. Nagol, E. F. Vermote, and S. D. Prince, "Effects of atmospheric variation on AVHRR NDVI data," *Remote Sens. Environ.*, vol. 113, pp. 392–397, 2009.

[47] Z. Wan, "New refinements and validation of the collection-6 MODIS land-surface temperature/emissivity product," *Remote Sens. Environ.*, vol. 140, pp. 36–45, 2014.

[48] H. Li *et al.*, "Temperature-based and radiance-based validation of the collection 6 MYD11 and MYD21 land surface temperature products over barren surfaces in northwestern China," *IEEE Trans. Geosci. Remote Sens.*, to be published, doi: 10.1109/TGRS.2020.2998945.

[49] A. Berk, G. Anderson, P. Acharya, and E. Shettle, "MODTRAN 5.2. 2 User's Manual, Spectral Sciences," Inc., Burlington, MA, USA, vol. 69, 2011.

[50] A. M. Baldridge, S. J. Hook, C. I. Grove, and G. Rivera, "The ASTER spectral library, Version 2.0," *Remote Sens. Environ.*, vol. 113, pp. 711–715, 2009.

[51] E. Borbas, S. W. Seemann, H.-L. Huang, J. Li, and W. P. Menzel, "Global profile training database for satellite regression retrievals with estimates of skin temperature and emissivity," in *Proc. 14th Int. ATOVS Study Conf.*, 2005, pp. 763–770.

[52] X. Xu, W. Fan, and L. Chen, "Matrix expression of thermal radiative characteristics for an open complex," *Sci. China Ser. D, Earth Sci.*, vol. 45, pp. 654–661, 2002.

[53] L. F. Chen, Z. L. Li, Q. H. Liu, S. Chen, Y. Tang, and B. Zhong, "Definition of component effective emissivity for heterogeneous and non-isothermal surfaces and its approximate calculation," *Int. J. Remote Sens.*, vol. 25, pp. 231–244, 2004.

[54] S. L. Ermida, I. F. Trigo, G. Hulley, and C. C. DaCamara, "A multi-sensor approach to retrieve emissivity angular dependence over desert regions," *Remote Sens. Environ.*, vol. 237, 2020, Art. no. 111559.

[55] J. A. Sobrino, G. Sòria, and A. J. Prata, "Surface temperature retrieval from along track scanning radiometer 2 data: Algorithms and validation," *J. Geophys. Res., Atmospheres*, vol. 109, pp. 1–8, 2004.

[56] C. Coll, J. M. Galve, R. Niclòs, E. Valor, and M. J. Barberà, "Angular variations of brightness surface temperatures derived from dual-view measurements of the advanced along-track scanning radiometer using a new single band atmospheric correction method," *Remote Sens. Environ.*, vol. 223, pp. 274–290, 2019.

[57] V. García-Santos, E. Valor, V. Caselles, M. Ángeles Burgos, and C. Coll, "On the angular variation of thermal infrared emissivity of inorganic soils," *J. Geophys. Res., Atmospheres*, vol. 117, pp. 1–18, 2012.

[58] Y. Yao *et al.*, "Bayesian multi-model estimation of global terrestrial latent heat flux from eddy covariance, meteorological and satellite observations," *J. Geophys. Res., Atmospheres*, vol. 119, pp. 4521–4545, 2014.